

Strong Purcell Effect in All-Dielectric Epsilon-Near-Zero Microcavities

Ali Panahpour,* Jussi Kelavuori, and Mikko Huttunen†

Photonics Laboratory, Physics Unit, Tampere University, FI-33014 Tampere, Finland

(Dated: February 16, 2024)

We theoretically study the quality and Purcell enhancement factors in epsilon-near-zero (ENZ) optical microcavities with ideally lossless or slightly lossy structures. In the case of ENZ rectangular cavities with perfect electric conductor (PEC) walls, our results supported by numerical simulations, show that both the quality and Purcell factors grow with increasing the length of cavity, having respective functional dependencies of n^{-3} and n^{-2} on the effective index of refraction, n . Further, we study extremely low-loss all-dielectric Bragg reflection waveguide cavities, near their cutoff frequencies. In such ENZ structures, the respective quality and Purcell factors scale as $(n\kappa)^{-1}$ and n/κ , in terms of real (n) and imaginary (κ) parts of the cavity effective index of refraction. We believe such structures exhibiting remarkably high quality ($\sim 10^6$) and Purcell factors ($\sim 10^3$), can drastically enhance various linear and nonlinear optical processes, and thus find use in applications ranging from laser development to optical sensing and metrology.

Epsilon-near-zero (ENZ) photonics provides a novel platform for developing new types of integrated photonic devices with unconventional functionalities [1–7]. This is due to variety of extraordinary effects, offered by ENZ materials and structures, such as energy squeezing [8], tunneling through subwavelength channels and bends [9], enhanced optical nonlocality and additional waves [10], control of spectral and directional emissivity [11], enhancement of optical nonlinearities [4], and boosting of the Purcell factor (PF) in radiative systems [7, 12–14].

Conventional ENZ materials or nanostructures have been mainly based on conducting oxide or nitride materials as well as metamaterials consisting of metal–dielectric or semiconductor–dielectric components [2, 3]. Perfect electric conductor (PEC) waveguides, and more realistic but lossy metallic waveguides, near their cutoff frequencies have also been utilized to emulate the properties of an ENZ medium [13]. However, most of the unique features of ENZ media are considerably deteriorated near optical frequencies due to internal dissipations caused by ohmic losses in conducting materials. In fact, conventional ENZ materials/structures usually exhibit rather low figure-of-merits (FoMs), defined as the ratio of real to imaginary part of effective permittivity, within their ENZ spectral range [15].

Several all-dielectric epsilon-mu-near-zero (EMNZ) architectures have been recently demonstrated to realize low-loss near-zero-index (NZI) metamaterials or photonic crystals [5, 16]. However, little work seems to exist on all-dielectric ENZ structures. Despite known challenges, such as poor transmission due to impedance mismatch between conventional and ENZ media, they also exhibit unique and highly advantageous properties. Notably, it has been shown that among the various sub-categories of NZI media including ENZ, mu-near-zero, and EMNZ (meta)materials, the PF diverges solely in the one-dimensional (1D) ENZ media, due to substantial growth of electromagnetic density of states (DOS) in such structures [17].

The ENZ-induced PF enhancement has been demonstrated both theoretically and experimentally in linear as

well as nonlinear systems [18–20]. However, full exploitation of the Purcell enhancement of radiative processes is severely restricted by optical losses of the ENZ structures. Importantly, this problem prevents further enhancement of spontaneous emission rate (SER) in ENZ media through coupling of embedded emitters to high-quality-factor (Q -factor) optical resonators. In fact, as we will show, such couplings in metal or semiconductor structures can result in suppression of high- Q resonances with no significant enhancement of radiative processes.

In this letter, we address the issue of conductor-induced ohmic losses by studying the Purcell effect and Q -factor in ENZ waveguides and microcavities formed by using all-dielectric Bragg reflection waveguides (BRWs). We show that these structures, operated near their cutoff frequencies, can provide a viable platform for experimental realization of low-loss ENZ microcavities. Furthermore, the studied ENZ cavities are predicted to result in scaling laws for Q - and Purcell factors that are different from those associated with conventional cavities. Our numerical results indicate the potential realization of cavities with Q -factors on the order of 10^6 . More importantly, our theoretical analysis suggests that such ENZ cavities could simultaneously exhibit high Purcell factors exceeding 10^3 .

The perturbative effect of structured vacuum on radiative processes, known as Purcell effect was originally demonstrated by coupling an emitter to a resonant cavity [21]. When the emission wavelength of the emitter is tuned to the resonant mode of a nondispersive cavity, the emission is enhanced by a factor of

$$F_P = \frac{6}{\pi^2} \left(\frac{\lambda}{2n} \right)^3 \frac{Q}{V}, \quad (1)$$

where λ is the photon wavelength in vacuum, n is the refractive index of medium inside the cavity, Q is the Q -factor of the cavity and V is the mode volume. The conventional approaches for enhancing the PF are mainly based on the development of three different classes of photonic structures: ultra-high- Q -factor dielectric microcavities with Q -factors in the range of 10^8 – 10^9 and mode volumes much larger than $(\lambda/2n)^3$ [22], photonic crystal nanocavities of moderate Q -factors (10^4 – 10^5) with mode volumes on the order of $(\lambda/2n)^3$ [23] and finally

* ali.panahpour@tuni.fi

† corresponding author: mikko.huttunen@tuni.fi

plasmonic nanoresonators having rather small Q -factors ($Q \leq 100$) but with mode volumes much smaller than $(\lambda/2n)^3$ [24]. Microcavities loaded with highly dispersive materials or structures have also been implemented for improving the cavity Q -factor [25, 26].

An intriguing idea to promote the Purcell effect is to load a cavity with high-FoM ENZ media. This presents a dual advantage by amplifying the unique features of ENZ media through cavity resonance as well as offering an additional mechanism for general enhancement of PF in optical resonators, based on ENZ characteristics rather than cavity features. Interestingly, due to the elongation of wavelengths in the ENZ region, ENZ cavities can potentially mitigate scattering-based losses caused by structural stress, imperfections, or defects. This property is of great practical importance as it alleviates a fundamental limitation frequently impeding the performance of high Q -factor microresonators [27].

To study the Purcell effect in ENZ structures in the weak interaction regime, we apply Fermi's golden rule giving the SER of a quantum emitter:

$$\Gamma = \frac{2\pi}{\hbar^2} |M_{12}|^2 g(\omega) \quad (2)$$

in terms of transition matrix element M_{12} and optical DOS $g(\omega)$. Applying the quantization procedure for a homogeneous and lossless dispersive medium [17, 28], the transition matrix element is given by:

$$|M_{12}|^2 = \frac{\hbar\omega}{2\varepsilon_0 V} \frac{|\mathbf{p}|^2}{n(\omega)n_g(\omega)}, \quad (3)$$

with n , n_g , V and \mathbf{p} being the (real part of) medium phase index, group index, quantization volume and emitter's dipole moment, respectively. A straightforward method to realize low-dimensional (in k -space) ENZ structures is to use metallic waveguides with planar or rectangular geometries, operating near their cutoff frequencies. In the case of a 1D rectangular waveguide with transverse dimensions of L_x and L_y , and with idealized PEC walls, the DOS for an arbitrary quantization length of L_z along z -axis is given by $g(\omega) = (L_z/\pi c)n_g(\omega)$. Thus, by using Eqs. (2) and (3), the SER of an emitter in the waveguide is given by:

$$\Gamma^W = \frac{|\mathbf{p}|^2}{\varepsilon_0 \hbar} \frac{1}{L_x L_y} \frac{\omega}{c} \frac{1}{n}, \quad (4)$$

and by normalizing it to the SER in free space, the PF turns into

$$F_P^W = \frac{3\pi}{L_x L_y} \frac{c^2}{\omega^2} \frac{1}{n}. \quad (5)$$

Now, we consider a single mode rectangular cavity, consisting of a vacuum-filled PEC waveguide with transverse dimensions of L_x and L_y , and a limited length of L_z . The resonance feedback along L_z is provided by reflections at the waveguide ports due to impedance mismatch between the ports and free space. We assume the cavity resonance mode is tuned to the emission frequency (ω_0) of a dipole emitter at the center of the cavity. In this condition, the DOS around the resonant

mode can be written as a normalized Lorentzian function of $g(\omega) = (2\delta\omega/\pi)/(4(\omega - \omega_0)^2 + \delta\omega^2)$, which exactly at resonance, reduces to $g(\omega_0) = (2/\pi)(Q/\omega_0)$. Here, $Q = \omega_0/\delta\omega$ is the Q -factor of the cavity with the resonance width of $\delta\omega$, which in terms of cavity finesse \mathcal{F} , is given by $Q = \mathcal{F}L_z\omega_0/\pi c$. Taking into account the cavity dispersion, particularly when resonance is near the cutoff frequency of the waveguide, the free spectral range is given by $c/2n_g L_z$ and the cavity Q -factor is scaled by the group index as Qn_g [25, 26]. Therefore, the DOS is accordingly determined by $g(\omega_0) = (2/\pi)(Q/\omega_0)n_g(\omega_0)$ and the SER in a dispersive single mode rectangular cavity is obtained as:

$$\Gamma^C = \frac{2|\mathbf{p}|^2 Q}{\hbar\varepsilon_0 V n}. \quad (6)$$

After normalizing to the SER in vacuum, the PF in terms of $\lambda_0 = 2\pi c/\omega_0$ fulfills:

$$F_P^C = \frac{3}{4\pi^2} \frac{\lambda_0^3 Q}{V n}. \quad (7)$$

Assuming $L_y = \lambda_0$ and L_x slightly larger than $\lambda_0/2$, which implies that the cavity resonance wavelength ($\lambda_0 = 2L_x/\sqrt{1 + (L_x/L_z)^2}$) is close to the cutoff wavelength ($\lambda_c = 2L_x$), and by using $Q = (2L_z/\lambda_0)\mathcal{F}$, we see from relation (7) that PF is proportional to the ratio \mathcal{F}/n . In the absence of material losses, the cavity finesse \mathcal{F} is determined by the reflectivity finesse, $\mathcal{F}_R = \pi\sqrt{R}/(1 - R)$ in terms of reflectivity of the ports, R . It can easily be shown that for NZI cavities, reflectivity finesse is proportional to n^{-1} . Therefore, the PF scales as n^{-2} and regarding the cavity fundamental resonance condition $n = \lambda_0/2L_z$, we find $F_P^C \propto (L_z/\lambda_0)^2$ and $Q \propto (L_z/\lambda_0)^3$. This is in contrast to the case of ordinary microcavities, where PF is reduced by increasing the mode volume.

Although relations (4) and (5) imply that SER and PF grow to infinity in lossless 1D structures at the frequency of zero effective index, the enhancement of radiative processes and PF is strongly limited by losses in real structures consisting of metallic or semiconductor components [17–20]. This deterioration is much more pronounced in resonant cavities when light propagates multiple times through the cavity structure. To demonstrate this effect in metallic cavities and compare it to the case of PEC-wall cavities, we conduct COMSOL simulations in wavelength domain, where we exploit the mathematical analogy of quantum and classical treatments of the SER. According to Poynting's theorem the radiated power of any current distribution $\mathbf{j}(\mathbf{r})$ with a harmonic time dependence in a linear medium must be equal to the rate of energy dissipation given by $dW/dt = -1/2 \int_V \text{Re} \{ \mathbf{j}^* \cdot \mathbf{E} \} dV$. For a current distribution corresponding to a point dipole emitter $\mathbf{j}(\mathbf{r}) = -i\omega\mathbf{p}\delta(\mathbf{r} - \mathbf{r}_0)$ with dipole moment \mathbf{p} located at \mathbf{r}_0 , the equation can be rewritten in terms of the electric dyadic Green function \mathbf{G} , as $dW/dt = \omega^3/2c^2\varepsilon_0\varepsilon \{ \text{Im} \{ \mathbf{p} \cdot \mathbf{G}(\mathbf{r}_0, \mathbf{r}_0; \omega) \cdot \mathbf{p} \} \}$, which establishes a link between the quantum and classical formalisms for the relative SER and PF calculations [29]. Following this approach, we place a gold nanoparticle carrying a harmonic current density, at the center of

the cavity, as an oscillating dipole emitter. Then we compute the power dissipation and normalize it to its corresponding value in free space, allowing us to determine the PF within the structures [30]. In Fig. 1, the PF curves are calculated for cavities formed by either PEC (solid curve) or gold (dashed curve) walls. The dimensions of the cavities are $L_x = 0.5 \mu\text{m}$, $L_y = 1 \mu\text{m}$, and $L_z = 8 \mu\text{m}$ and the dipole moment of the emitting nanoparticle is along y -axis, exciting the lowest order TE mode of the cavity. For the case of gold cavity, L_x is reduced by the value of skin depth to keep the cutoff at $\lambda_c = 1 \mu\text{m}$ (the effective thickness of the waveguide is larger than the distance between the walls due to some penetration of waves into metallic walls). The resonance feedback is provided by impedance mismatch through incorporating two waveguide sections filled with materials of refractive index $n = 2$ at the cavity ports. The curves show

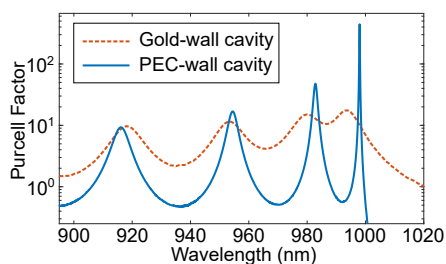


FIG. 1. Numerically calculated PFs for cavities with $L_x = 0.5 \mu\text{m}$, $L_y = 1 \mu\text{m}$, $L_z = 8 \mu\text{m}$ and cutoff wavelength of $\lambda_c = 1 \mu\text{m}$, for PEC (solid curve) and gold (dashed curve) cavity walls.

that the free spectral range and spectral width of the resonances are reduced in both PEC and gold-wall resonators, when approaching the cutoff wavelength. This is due to increased dispersion inside the cavities near the cutoff wavelength. However, the Q -factor and PF of the gold cavity are considerably lower than those of the PEC cavity, due to the ohmic losses of gold. The losses also detrimentally affect the dispersion profile of modes in a waveguide. As depicted in Fig. 2a, the dispersion of the real part of effective index, $n(\omega)$ and consequently the group index (being proportional to the derivative of $n(\omega)$ or $n^{-1}(\omega)$) in a PEC waveguide tends to infinity when approaching the cutoff wavelength of $\lambda_c = 1 \mu\text{m}$. However, for a gold-wall waveguide (Fig. 2b), the group index is maximized already before the cutoff and gradually tends to zero at longer wavelengths. In this case, losses (corresponding to imaginary part of effective index, $\kappa(\omega)$) grow gradually before the cutoff and increase abruptly by passing through the cutoff wavelength.

In Figs. 3a and 3b, the results of COMSOL simulations are demonstrated, to show the functional dependence of PF and Q -factor (blue dots) on the effective index of refraction ($n = \lambda_0/2L_z$) in a PEC-wall cavity, through changing the cavity length, L_z . The resonance feedback is provided by the same method as in Fig. 1. The computed PF values differ from those obtained from Eq. 7 by a factor of around six, mainly due to the smaller value of the effective cavity mode volume, compared to the geometrical volume used in Eq. 7. The straight lines in Fig. 3, correspond to different functional dependence on

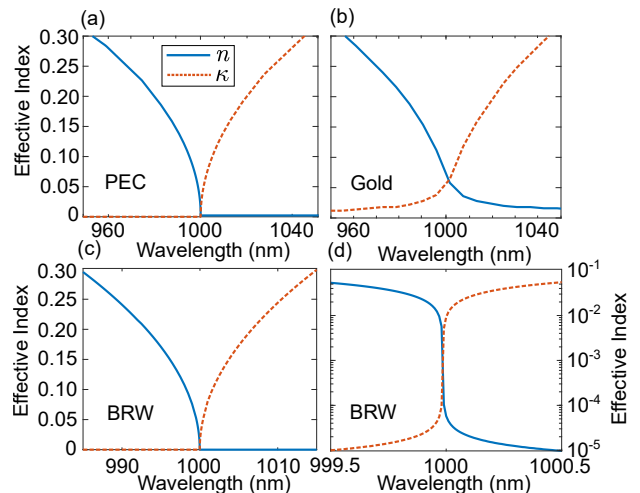


FIG. 2. Dispersion curves of (a) a PEC waveguide, (b) a gold-wall waveguide and (c) a BRW around the cutoff wavelength of $\lambda_c = 1 \mu\text{m}$. The transverse dimensions of the PEC and gold wall waveguides are the same as in Fig. 1. (d) A magnified view of the BRW dispersion curve near the cutoff wavelength, shown in logarithmic scale.

$1/n$. Clearly, the simulation results confirm the scaling of PF and Q -factor as n^{-2} and n^{-3} , respectively.

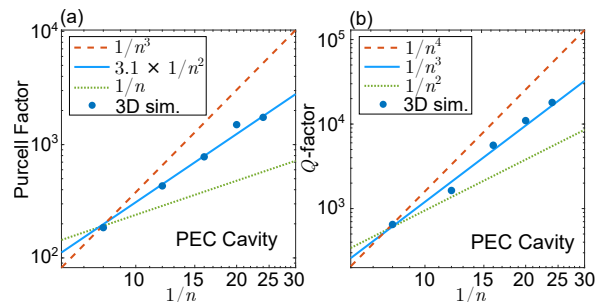


FIG. 3. Simulation results (blue dots) showing (a) PF and (b) Q -factor values in PEC-wall cavities with $L_x = 0.5 \mu\text{m}$, $L_y = 1 \mu\text{m}$, and $L_z = 4, 6, 8, 10, 12 \mu\text{m}$, corresponding to $1/n \approx 8, 12, 16, 20$ and 24 , respectively. The lines represent different functional dependence of PF and Q -factor on $1/n$.

In practice, perfectly lossless counterparts of ENZ PEC waveguides and cavities do not exist. However, by utilizing all-dielectric planar BRWs [31] operating near their cutoff frequencies, one can potentially realize extremely low-loss ENZ structures. Enhanced group index has been studied in near-cutoff BRWs with focus on the associated slow-light features [32, 33]. The guided waves in such structures propagate parallel to the Bragg walls with very little losses compared to common ENZ structures. In principle, the radiative losses through the Bragg walls can be arbitrarily reduced by increasing the number of cladding layers. Therefore, the supported low-loss waveguide modes show strong dispersion and large group indices ($n_g \approx n^{-1}$) near the cutoff frequencies [34–36], behaving thus very similar to PEC waveguides (Figs. 2a and 2c). The dispersion curves in Fig. 2c are obtained by two-dimensional (2D) COMSOL mode analysis simulation of a planar quarter-wave BRW with infinite lateral dimen-

sions. The electric field polarization of the mode is parallel to the Bragg reflectors and perpendicular to the propagation direction. The waveguide core material is assumed to be a Borosilicate glass and the cladding structures on each side was taken to consist of 20 pairs of alternative Borosilicate and TiO_2 layers, with phase thicknesses of $\pi/2$ and refractive indices of $n_{\text{BK7}} = 1.51 + i9.93 \times 10^{-9}$ [37] and $n_{\text{TiO}_2} = 2.31 + i10^{-6}$ [38]. The magnified view of the BRW dispersion curve in Fig. 2d shows that the FoM of the waveguide at $\lambda = 999.5$ nm is as high as $\epsilon'/\epsilon'' = n^2 - \kappa^2/2n\kappa \approx 2677$, with $n = 0.053$ and $\kappa = 9.9 \times 10^{-6}$ as the real and imaginary parts of the effective index. The Q -factor of a waveguide with negligible dispersion would be also given by the same above ratio ($Q = \epsilon'/\epsilon''$). However, for a dispersive and low-loss medium, such as the high-FoM BRW, near its cutoff wavelength, the Q -factor is estimated as [36, 39]:

$$Q^{\text{W}} \approx \frac{1}{2\epsilon''} \frac{\partial[\omega\epsilon'(\omega)]}{\partial\omega} \approx \frac{1}{2n\kappa}, \quad (8)$$

To derive the above relation, the Drude model is used (representing a dispersive and absorptive medium) in the limit of negligible damping constant ($\gamma \ll \omega$). For the above-described BRW, this estimation yields: $Q^{\text{W}} \approx 9.53 \times 10^5$ at $\lambda = 999.5$ nm.

In planar ENZ BRWs with finite lateral dimensions (Fig. 4a), there are additional radiative losses through the lateral sides of the waveguide (along y - and z -directions). In ENZ waveguides, due to lower effective

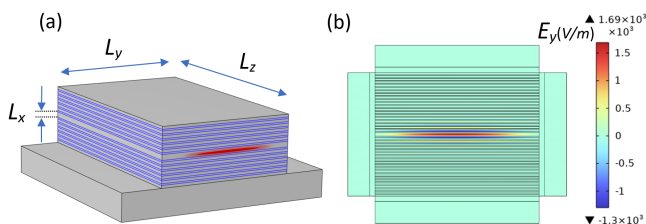


FIG. 4. (a) Schematic view of a BRW with finite lateral sizes and (b) its transverse cross-section view, showing the y -component of electric field, corresponding to an ENZ mode of the waveguide, computed by 2D mode-analysis simulation.

index of the core with respect to cladding and free space, the guiding mechanism is different from that in conventional dielectric waveguides based on total internal reflection. In contrast, the structure supports leaky modes and guidance is achieved by partial reflections from the Bragg or lateral walls. While the reflection from the Bragg walls is caused by destructive interference of waves in the cladding layers, reflection from the side walls is due to large impedance mismatch between the core and surrounding free space. Thus, a planar BRW with finite lateral dimensions acts like a 3D cavity.

We assume that the propagation of y -polarized waves corresponding to the cavity ENZ mode is along the z -axis shown in Fig. 4a. Therefore, the cavity output coupling is taken to be along z -axis, and optical leakage along x and y directions are considered as the radiative losses of the waveguide. Our mode-analysis simulations approve the reduction of radiative losses along y -direction by increasing the cavity width, L_y . Namely, for a BRW with

the same parameters used in Fig. 2c, but with the limited lateral width of $L_y = 10$ μm , the mode analysis simulation gives an effective index of $n = 0.047 + i1.29 \times 10^{-5}$, at $\lambda = 999.5$ nm, corresponding to FoM of 1828 (Fig. 4b). By increasing the width to 15 μm and 20 μm , the FoM grows to 2483 and 2621 correspondingly, approaching to the value obtained for the laterally infinite structure of Fig. 2c. This implies that by increasing the cavity width, the associated lateral dissipation reduces to amounts comparable or even smaller than leakage through the finite Bragg walls. The cavity Q -factor, corresponding to output coupling, represented by Q^{out} , can be enhanced by increasing the cavity length and subsequent reduction of the effective index ($n = \lambda_0/2L_z$). However, the overall Q -factor of the cavity is also affected by the waveguiding structure through the relation $1/Q = 1/Q^{\text{W}} + 1/Q^{\text{out}}$. Regarding the waveguide radiative losses through the finite Bragg reflectors and side walls, as well as material losses of the structure, the overall Q -factor is limited by Q^{W} , determined in equation (8).

For numerical assessment of Q^{W} , we consider the same BRW structure related to Fig. 2c and calculate the transmission through the structure, when illuminated by an incident wave propagating perpendicular to the Bragg walls. The incident wave is spectrally centered around the waveguide cutoff frequency with its electric field polarization parallel to the Bragg walls. Regarding the wave normal incidence, a mode with a zero effective index is developed in the core, at the waveguide cutoff wavelength. This mode exhibits no propagation in the waveguide core along the Bragg walls, resulting in zero group velocity. The BRW acts like a quarter-wave-shifted distributed feedback resonator or simply as a Fabry-Pérot resonator, composed of two Bragg reflectors with a half-wave-thickness core in between. The core serves as a local defect in a crystal lattice, generating a local state at the center of the stop-band (bandgap) (Fig. 5a). A transmission peak emerges as a result of multiple wave reflections from the Bragg reflectors. The waveguide Q -factor is calculated by measuring the spectral width of the transmission peak. The ENZ modes in the BRW, associated with wavelengths smaller than the cutoff wavelength are established in a similar manner, when the structure is illuminated by waves having slightly non-zero incidence angles. In this condition, the waves successively reflect off the Bragg walls and exhibit a slow propagation characterized by a very small wave-vector component along the direction of propagation (small phase index n , and large group index, $n_g \approx n^{-1}$). As the angle of incidence increases, the transmission peak experiences a blue shift, while the waveguide Q -factor is on the same order of magnitude as in the case of normal incidence. The COMSOL simulation results representing the resonant transmission peaks for the condition of normal incidence are shown in Fig. 5b, for three different number of alternative Borosilicate and TiO_2 layers. We obtain $Q^{\text{W}} \approx 4.5 \times 10^5$, 8.5×10^5 and 2.5×10^6 , corresponding to $N = 16$, 18 and 20 pairs of layers. The Q -factor is enhanced by increasing the number of layers, but the visibility of the transmitted wave is dramatically reduced. As expected, the Q -factor corresponding to $N = 20$ is of the same order of magnitude estimated in relation (8).

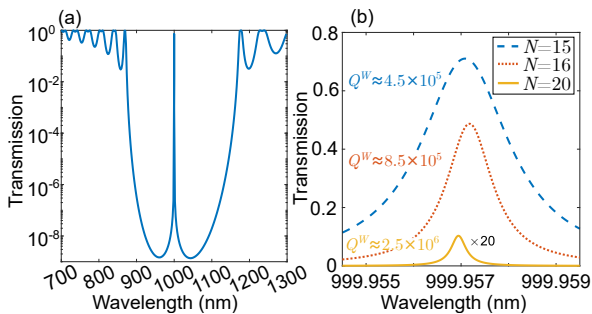


FIG. 5. Perpendicular transmission through the BRW with parameters as in Fig. 2c, with electric field polarization parallel to the Bragg walls. (a) Transmission corresponding to the number of cladding pairs of $N = 15$, (b) and a zoom up view of transmission peak for $N = 15, 16$ and 20 , represented by dashed, dotted and solid curves, respectively.

For estimating the PF of a BRW cavity, we apply Eq. (7) and take L_x slightly larger than $\lambda_0/2n_{\text{core}}$ (n_{core} is the real part of the BRW core material), $L_z = \lambda_0/2n$ and $L_y \approx \lambda_0/2n$ (not exactly equal to $\lambda_0/2n$ to ensure a single resonant mode along z -axis). We obtain $F_P^{\text{BRWC}} \approx (6n^2n_{\text{core}}/\pi^2)(Q/n)$, where Q/n (almost equivalent to Qn_g) represents the Q-factor of the disper-

sive cavity. Replacing the Q/n by the limiting Q-factor of the cavity from relation (8) we obtain:

$$F_P^{\text{BRWC}} \approx \frac{3n_{\text{core}}}{\pi^2} \frac{n}{\kappa}, \quad (9)$$

which for $n = 0.053$ and $\kappa = 9.9 \times 10^{-6}$, corresponding to the assumed BRW cavity, and $n_{\text{core}} = 1.51$ associated with the borosilicate core, results in $F_P^{\text{BRWC}} \approx 2457$. This typical value is two orders of magnitude greater than the PF we obtained for the gold-wall cavity in Fig. 1, and almost three orders of magnitude higher than radiation enhancement factors experimentally achieved in plasmonic ENZ structures [19, 20]. However, numerical assessment of relation (9) through 3D simulation of BRW microcavities, having dimensions much larger than wavelength (in free space), poses challenges due to the substantial computational workload and more critically, serious convergence issues.

In summary, we derived scaling laws for quality and Purcell factors in lossless microcavities, revealing their growth with increasing the length of cavity. In addition, all-dielectric BRWs, operating near their cutoff frequencies are introduced as building blocks of high-FoM ENZ microcavities to harness and amplify the unique ENZ features, through significant enhancement of both quality and Purcell factors in such microcavities.

-
- [1] N. Engheta, *Science* **340**, 286 (2013).
[2] X. Niu, X. Hu, S. Chu, and Q. Gong, *Adv. Opt. Mater.* **6**, 1701292 (2018).
[3] J. Wu *et al.*, *Photonics Research* **9**, 1616 (2021).
[4] O. Reshef *et al.*, *Nature Reviews Materials* **4**, 535 (2019).
[5] N. Kinsey, C. DeVault, A. Boltasseva, and V. M. Shalaev, *Nat. Rev. Mater.* **4**, 742 (2019).
[6] M. Lobet *et al.*, *ACS photonics* **10**, 3805 (2023).
[7] I. Liberal and N. Engheta, *Nature Photonics* **11**, 149 (2017).
[8] A. Alù and N. Engheta, *Physical Review B* **78**, 035440 (2008).
[9] M. Silveirinha and N. Engheta, *Physical Review Letters* **97**, 157403 (2006).
[10] R. J. Pollard *et al.*, *Physical Review Letters* **102**, 127405 (2009).
[11] J. S. Hwang *et al.*, *Advanced Materials* **35**, 2302956 (2023).
[12] A. Alù and N. Engheta, *Physical Review Letters* **103**, 043902 (2009).
[13] A. Alù and N. Engheta, *Materials* **4**, 141 (2011).
[14] R. Fleury and A. Alu, *Physical Review B* **87**, 201101 (2013).
[15] M. Javani and M. Stockman, *Physical review letters* **117**, 107404 (2016).
[16] Y. Li *et al.*, *Light: Science and Applications* **10**, 203 (2021).
[17] M. Lobet *et al.*, *ACS Photonics* **7**, 1965 (2020).
[18] E. J. R. Vespeur *et al.*, *Physical Review Letters* **110**, 013902 (2013).
[19] J.-K. So *et al.*, *Applied Physics Letters* **117**, 181104 (2020).
[20] V. Caligiuri *et al.*, *ACS photonics* **5**, 2287 (2018).
[21] E. M. Purcell, H. C. Torrey, and R. V. Pound, *Physical Review* **69**, 37 (1946).
[22] T. J. Kippenberg *et al.*, *Applied Physics Letters* **85**, 6113 (2004).
[23] Y. Akahane *et al.*, *Nature* **425**, 944 (2003).
[24] F. Wang and Y. R. Shen, *Physical Review Letters* **97**, 206806 (2006).
[25] M. Soljačić *et al.*, *Physical Review E* **71**, 026602 (2005).
[26] G. Gao *et al.*, *Scientific Reports* **6**, 19999 (2016).
[27] T. J. Kippenberg *et al.*, *Applied Physics Letters* **83**, 797 (2003).
[28] P. W. Milonni, *Journal of Modern Optics* **42**, 1991 (1995).
[29] L. Novotny and B. Hecht, *Principles of nano-optics* (2012).
[30] Y. Chen *et al.*, *Physical Review B* **81**, 125431 (2010).
[31] P. Yeh and A. Yariv, *Optics Communications* **19**, 427 (1976).
[32] G. G. Kozlov *et al.*, *Optics and Spectroscopy* **109**, 397 (2010).
[33] A. Fuchida *et al.*, *Japanese Journal of Applied Physics* **51**, 050203 (2012).
[34] B. Nistad, M. W. Haakestad, and J. Skaar, *Optics Communications* **265**, 153 (2006).
[35] Y. Xu *et al.*, *Journal of Lightwave Technology* **20**, 428 (2002).
[36] R. Loudon, *Journal of Physics A: General Physics* **3**, 233 (1970).
[37] Schott, <http://www.schott.com> (2023), accessed: November, 2023.
[38] S. V. Zhukovsky *et al.*, *Physical Review Letters* **115**, 177402 (2015).
[39] F. D. Nunes *et al.*, *JOSA B* **28**, 1544 (2011).
[40] P.-f. Qiao *et al.*, *Physical Review A* **83**, 043824 (2011).